sustainability

MDPI

Article

Waste Stone Wool as a Co-Precursor in Natural Pozzolan-Based Alkali-Activated Materials: Balancing Performance, Resource Efficiency, and Carbon Intensity

Kübra Ekiz Barış

Faculty of Architecture and Design, Kocaeli University, 41300 Kocaeli, Türkiye; kubra.ekizbaris@kocaeli.edu.tr

Abstract

Within the literature reviewed, no systematic study was identified that evaluates waste stone wool (SW) as a partial replacement for natural pozzolan (NP) while varying both SW content and NaOH concentration in the same alkali-activated material (AAM) mixture. To address this gap, this study examined SW replacement levels of 0–40 wt.% and NaOH concentrations of 5, 7.5, and 10 M. Fresh-state behavior, physical and mechanical properties, drying shrinkage, pore structure, and material-based environmental indicators were evaluated. Increasing SW replacement level reduced flowability, while mixtures containing up to 30% SW showed improved hardened-state performance. SW30-7.5M exhibited the best overall performance, with compressive and flexural strengths of 16.13 and 3.41 MPa, respectively, total porosity of 15.07%, and ultrasound pulse velocity of 3.19 km/s. It also showed the lowest 63-day drying shrinkage magnitude, with a reported value of -1014.9×10^{-6} mm/mm. Mercury intrusion porosimetry (MIP) analysis of this mixture gave an MIP porosity of 14.03% and an average pore diameter of 0.24 μm. X-ray diffraction (XRD) and Fourier transform infrared spectroscopy (FTIR) indicated changes in the bonding environment after activation, but did not identify a specific reaction product or a new dominant crystalline phase. Within the defined material-input boundary, SW replacement reduced NP consumption and the material-based carbon indicator, with the lowest carbon intensity per unit compressive strength (0.0113 kg CO_2-eq./MPa) obtained for SW30-7.5M. The overall performance of the investigated AAMs depended on the combined effects of SW replacement level and NaOH concentration.

Keywords: alkali-activated material; stone wool waste; natural pozzolan; sodium hydroxide activation; pore structure

Check for updates

Academic Editor: Paulo Ferrão

Received: 24 September 2026
Revised: 23 October 2026
Accepted: 30 October 2026
Published: 4 November 2026

Copyright: © 2026 by the author. Licensee MDPI, Basel, Switzerland. This article is an open access article distributed under the terms and conditions of the Creative Commons Attribution (CC BY) license.

1. Introduction

The environmental impacts associated with conventional construction materials have prompted growing interest in alternatives to Portland cement and in the valorization of waste materials as a construction resource. Alkali-activated materials (AAMs) represent one such alternative. They can be produced from a wide range of aluminosilicate-rich sources; however, their environmental performance is not automatically better simply because Portland cement is absent from the mixture. Precursor origin, transportation distance, and the type of alkaline activator used can substantially influence the overall environmental performance. Therefore, the environmental benefits of AAMs depend on the overall material composition rather than on cement replacement alone [1,2].

Mineral wool waste (MWW) is a relevant waste stream for this type of application. It mainly consists of stone wool (SW) and glass wool (GW), which are commonly used for thermal insulation in buildings. Once discarded, however, their physical characteristics create practical handling and disposal challenges. Because the material is very light and bulky, even a relatively small mass occupies a substantial volume. Its fibrous structure also makes handling, transport, storage, and disposal more complex and costly [3,4]. Reuse is still limited, so incorporating MWW into construction materials may help reduce the volume of waste requiring storage or final disposal.

Estimating the amount of mineral wool waste generated in the European Union (EU) is difficult because the available data are fragmented. Based on Eurostat data and the literature, Väntsi and Kärki estimated approximately 2.4 million tonnes of end-of-life mineral wool waste in the EU-27, including stone wool and glass wool [5]. This estimate concerns waste from the building stock and should therefore be distinguished from manufacturing waste.

A 2021 pre-feasibility report prepared by the Karacadağ Development Agency states that, as of 2020, the combined annual installed capacity of the nine major stone wool manufacturers in Türkiye was 493,000 tonnes [6]. FAS Hansek, a provider of recycling systems for the stone and glass wool industries, reports that edge-trim waste from mineral wool production may account for approximately 6–8%, with product residues and unsold products adding a further 5–8% of production [7]. The company states that total unsold production may reach approximately 5–15% and gives 6% as a conservative example for a stone wool production line. Applying this 6% waste rate to the installed capacity of 493,000 tonnes per year yields an estimated 29,580 tonnes per year of production residues or unsold products.

The chemical composition of SW is another reason it has been considered for use in AAMs. SW typically contains SiO_2, Al_2O_3, CaO, and MgO, and a substantial proportion of its structure is amorphous. This means that it may participate in reactions under alkaline conditions instead of behaving only as an inert addition [8]. Differences in the chemical compositions of SW and GW can lead to different reaction products during alkali activation. Yliniemi et al. [8] observed amorphous C-(N)-A-S-H-type phases in an SW-based AAM activated with NaOH and sodium silicate. Their results also suggest that the activator has a significant influence on the resulting structure.

Previous studies on mineral wool (MW)-based AAMs have examined SW both as a sole precursor and as part of broader AAM formulations containing SW and/or GW. Across these studies, MW has been used as the main precursor, as a co-precursor, or as a fibrous addition in mixtures containing slag, metakaolin, or fly ash [9–12]. Its influence depends not only on the amount incorporated into the mixture but also on the activation conditions. Previous studies have shown that its addition may alter strength, pore characteristics, fresh-state behavior, and dimensional stability [4,13]. At moderate replacement levels, some studies have reported improvements in flexural response and shrinkage behavior. Effects on fresh-state behavior vary with mixture composition and processing conditions. Higher replacement levels may reduce compressive strength through increased porosity, fiber agglomeration, or matrix defects [4,12]. For example, Luo and Yu [12] investigated MWW contents of 0–12 wt.% in a Class F fly-ash geopolymer and reported changes in geopolymerization, pore structure, compressive strength, flexural properties, and drying shrinkage. Because their activator parameters were kept constant, their results do not establish how SW replacement interacts with NaOH concentration in an NP-based mixture.

The type of alkali activator also affects the behavior of MW-based materials. Yliniemi et al. [14] directly compared NaOH, sodium silicate, sodium aluminate, and sodium carbonate and showed that activator type strongly affects the reaction kinetics, setting time, and compressive strength development. NaOH activation of SW has been associated with

rapid reaction, fast setting, and high early strength [14]. Therefore, NaOH concentration and activator composition are important design variables in mixtures containing SW. Because alkaline activators contribute to the environmental burden of AAMs, systematic evaluation of NaOH-based mixtures without sodium silicate is also environmentally relevant [15]. Najimi et al. [16] found that the optimum natural-pozzolan (NP)/slag binder combination and NaOH concentration were interdependent for compressive strength, while also assessing flow, setting time, hydration heat, absorption, chloride penetration, and drying shrinkage. Adewumi et al. [17] varied NaOH concentration from 4 to 14 M in NP/limestone mortars activated with a NaOH–sodium-silicate blend and reported effects on strength, bond properties, reaction products, and microstructure. Taken together, these studies motivate joint consideration of precursor composition and alkali concentration. The direct evidence for their interdependence comes from Najimi et al. [16], whereas Adewumi et al. [17] provide complementary evidence that NaOH concentration affects the performance of NP-containing mortar. Neither study predicts the optimum for the NaOH-only NP–SW mixtures examined here.

NPs are also considered potential precursors for AAMs [18]. Geological studies document volcanic terrains and tuff deposits in several regions of Türkiye [19,20]. One study reports that Tertiary- and Quaternary-age volcanic rocks cover approximately 155,000 km^2. Other studies have assessed tuffs from Central Anatolia and Trabzon–Bayburt for their suitability as NPs for cementitious use [19,20]. The reported area refers to volcanic rocks, not to a quantified reserve of standards-compliant or economically recoverable NP; suitability must therefore be established for each deposit. The Gelincik tuff from Isparta used in this study was selected as a volcanic precursor sourced in Türkiye, and its pozzolanic suitability was evaluated against TS 25:2008/T1 [21,22]. Another study investigated Cappadocia excavation waste as an NP for alkali activation [23]. Together, these studies provide regional context for examining a Turkish-sourced volcanic precursor in a system for valorizing SW, without implying a transport advantage between the two material sources.

Previous studies have investigated waste SW as the sole precursor or as a component of AAM formulations containing mineral wool, slag, fly ash, or metakaolin [9–14]. Other studies have examined NaOH concentration in NP-containing binders [16,17]. However, the literature review conducted for this study did not identify a systematic investigation in which SW was used specifically as a partial replacement for NP while both the SW replacement level and NaOH concentration were varied within the same experimental matrix. Therefore, how the properties of NaOH-activated NP–SW-based AAMs vary across these mixture combinations remains insufficiently documented.

To address this gap, this study evaluates NP-based AAMs prepared with SW replacement levels of 0–40 wt.% and NaOH concentrations of 5, 7.5, and 10 M. The investigation covers flowability, setting behavior, physical and mechanical properties, drying shrinkage, mass loss, and pore structure. MIP, XRD, and FTIR analyses were used to characterize pore structure and changes associated with activation. The study also evaluates mechanical performance alongside natural precursor consumption and material-based carbon indicators. Its primary contribution is an integrated assessment of these fresh-state, hardened-state, structural, dimensional-stability, and material-related environmental properties.

2. Materials and Methods

2.1. Raw Materials

The NP used in this study was a volcanic tuff sourced from the Gelincik region of Isparta, Türkiye. The deposit is associated with the Gölcük volcanic field in southwestern Anatolia, whose lithological units include trachyte, trachyandesite, andesite, volcanic tuff, and pumice [21]. The pozzolanic suitability of the NP was evaluated in accordance with TS

25:2008/T1 [22]. The combined SiO_2 + Al_2O_3 + Fe_2O_3 content was 82.51 wt.%, exceeding the minimum requirement of 70 wt.% specified in the standard. In addition, the 7-day flexural and compressive strengths were 1.85 and 9.2 MPa, respectively, both exceeding the corresponding minimum requirements of 1.0 and 4.0 MPa. These results confirmed that the volcanic tuff satisfied the pozzolanic requirements specified in the standard [22]. The combined SiO_2 + Al_2O_3 + Fe_2O_3 content of SW was below the 70 wt.% limit specified in TS 25 for NPs; therefore, SW was not evaluated as a TS 25-compliant NP. However, this compositional criterion alone does not determine the potential reactivity of SW under alkali-activation conditions. This reactivity was not directly measured in the present study and should be investigated in future work.

Waste SW was collected as a source-separated production and cutting residue from a SW manufacturing facility in Dilovası, Kocaeli, Türkiye. To remove free moisture, the SW was first oven-dried at 100 °C for 24 h. The dried SW was then ground for 6 h using a laboratory-scale tumbling ball mill (MEDI TMA, Kocaeli, Türkiye). Following grinding, the material was sieved to obtain particles smaller than 63 µm and homogenized prior to use.

In this study, SW was ground for 6 h in a tumbling ball mill as a laboratory-scale pretreatment to obtain a reproducible SW powder fraction below 63 µm. This duration was not optimized for industrial throughput, and the specific energy demand of grinding was not measured. Previous studies have examined different comminution approaches for mineral wool, including cutting, crushing, and grinding; however, the selected treatment can affect the resulting fibre dimensions and morphology [3,15]. For scale-up, a staged process involving coarse cutting or shredding followed by appropriately selected milling and particle-size classification could be evaluated. This process route was not tested in the present study, and its ability to achieve the required particle-size range, reduce processing energy, and maintain the desired AAM performance remains to be verified.

The particle size distributions of NP and SW were determined using a Mastersizer 3000 laser particle size analyzer (Malvern Panalytical, Malvern, UK), and the results are presented in Figure 1. SW exhibited a finer particle size distribution than NP, with median particle sizes (d_{50}) of 18.25 and 32.47 µm, respectively. The corresponding d_{10} and d_{90} values are provided in Figure 1.

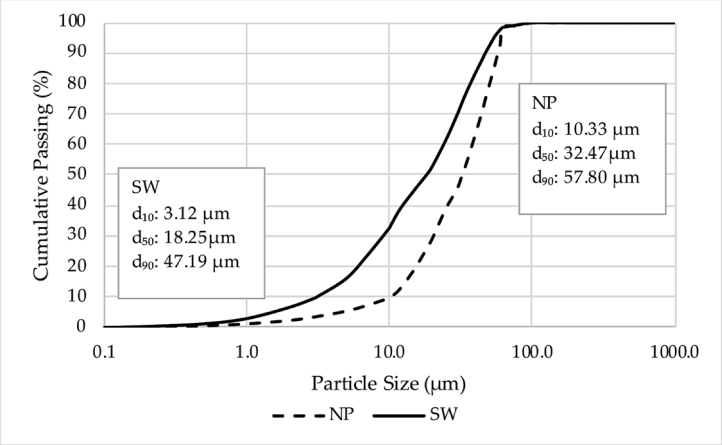


Figure 1. Particle size distributions of NP and SW.

The true densities of NP and SW were determined using a helium gas pycnometer (AccuPyc II 1340, Micromeritics, Norcross, GA, USA) and were found to be 2.55 and 2.72 g/cm^3, respectively. The chemical compositions of NP and SW were determined using a Philips PW-2404 wavelength-dispersive X-ray fluorescence (XRF) spectrometer (Philips Analytical B.V., Almelo, The Netherlands), and the results are presented in Table 1. NP was

rich in SiO_2 (60.32 wt.%) and Al_2O_3 (18.98 wt.%), whereas SW exhibited comparatively higher contents of CaO (17.2 wt.%) and MgO (10.6 wt.%).

Table 1. XRF chemical compositions of NP and SW.

Oxide	NP (wt.%)	SW (wt.%)
SiO_2	60.32	39.5
Al_2O_3	18.98	17.5
CaO	4.74	17.2
MgO	1.97	10.6
Fe_2O_3	3.21	8.8
TiO_2	0.56	1.2
Na_2O	3.56	1.0
K_2O	3.91	0.7
SO_3	0.25	0.2
P_2O_5	0.1	0.1
LOI	2.4	3.2

NaOH pellets (molar mass: 40 g/mol) supplied by Merck Chemicals were used as the sole alkaline activator. Previous AAM studies have examined a range of NaOH concentrations, including 4, 8, and 12 M for tuff-based bricks [24], 4–14 M for NP/limestone mortars activated with a NaOH–sodium-silicate blend [17], and 8 M for volcanic-ash-based materials [25]. Informed by these reported ranges, 5, 7.5, and 10 M NaOH were selected to examine the effect of activator concentration in the NP–SW mixtures. The 7.5 M level was included as an intermediate concentration between 5 and 10 M. For each NaOH concentration, the required amount of NaOH was dissolved in deionized water and the final solution volume was adjusted to 1 L. Thus, 200, 300, and 400 g of NaOH were used for the 5, 7.5, and 10 M solutions, respectively. The solutions were prepared 24 h before mixing and stored in sealed containers at ambient temperature until use, allowing them to cool.

2.2. Mixture Design

In this study, a two-variable mixture design was established to systematically evaluate the effects of the SW replacement level and NaOH concentration on the properties of NP-based AAMs. SW was used to replace NP at levels of 0%, 10%, 20%, 30%, and 40% by mass, and each precursor composition was activated using 5, 7.5, and 10 M NaOH solutions. Thus, a total of 15 mixtures were prepared, covering five SW replacement levels and three different NaOH concentrations. The mixture compositions are presented in Table 2.

In all mixtures, the activator-to-precursor ratio was kept constant at 0.40, and the water-to-precursor ratio at 0.35. Accordingly, 480 g of the prepared NaOH solution was used per 1200 g of total precursor. The 480 g portions of the prepared 5, 7.5, and 10 M NaOH solutions contained 81, 114, and 144 g of solid NaOH, respectively. Since varying the NaOH concentration also alters the water content of the prepared solution, the amount of additional deionized water was adjusted according to the NaOH concentration to maintain a constant total water content across all mixtures. Specifically, 21, 54, and 84 g of additional deionized water were used for the 5, 7.5, and 10 M series, respectively, thereby keeping the total water content fixed at 420 g for each mixture. Accordingly, the water-to-precursor ratio of 0.35 was calculated using the total water from both the NaOH solution and the additional deionized water. No further water adjustments were made as a function of SW replacement level. These ratios were selected based on preliminary mixing trials and comparable water-to-precursor and activator-to-precursor ratios reported for NaOH-activated MW-based AAMs. Pavlin et al. [13] used a water-to-precursor ratio of 0.35 and an

activator-to-precursor ratio of 0.43 in a NaOH-activated SW-based AAM; Yliniemi et al. [8] also reported a water-to-precursor ratio of 0.35 for a NaOH-activated SW-based AAM.

No sand or other aggregate was incorporated into the mixtures; the investigated materials consisted of the NP–SW precursor blend and the alkaline activator.

Table 2. Mixture proportions of NP-SW-based AAMs.

Mixture	NP (g)	SW (g)	NaOH Concentration	NaOH Solution (G)	Additional Water (G)	Water-to-Precursor Ratio	Activator-to-Precursor Ratio
SW0-5M	1200	0	5 M	480	21	0.35	0.40
SW0-7.5M			7.5 M		54		
SW0-10M			10 M		84		
SW10-5M	1080	120	5 M		21		
SW10-7.5M			7.5 M		54		
SW10-10M			10 M		84		
SW20-5M	960	240	5 M		21		
SW20-7.5M			7.5 M		54		
SW20-10M			10 M		84		
SW30-5M	840	360	5 M		21		
SW30-7.5M			7.5 M		54		
SW30-10M			10 M		84		
SW40-5M	720	480	5 M		21		
SW40-7.5M			7.5 M		54		
SW40-10M			10 M		84		

2.3. Specimen Preparation and Curing

For each mixture, NP and SW were weighed in the proportions specified in Table 2, and the dry components were mixed using a mechanical mixer at 60 rpm for 2 min. Subsequently, the NaOH solution at the corresponding concentration and the required amount of additional deionized water were added, and mixing continued at the same speed for an additional 3 min. The fresh mixtures were cast into lubricated 40 × 40 × 160 mm prismatic molds. After casting, the molds were covered with polyethylene film.

Nine 40 × 40 × 160 mm prisms were prepared for each mixture. Three specimens were used for physical tests, three for mechanical tests, and the remaining three for drying shrinkage and mass measurements. The specimens remained in the covered molds for 24 h at 24 ± 2 °C. They were then demolded and cured at 24 ± 2 °C and 50 ± 5% relative humidity. Ambient curing was selected to assess whether the NP–SW mixtures could harden at room temperature without externally supplied heat, a condition relevant to potential building-material applications. The study was not designed to compare ambient and heat-curing regimes; therefore, the results do not establish ambient curing as the optimum curing method or rule out possible strength gains under heat curing. Physical, mechanical, and microstructural tests were carried out at 28 days. The specimens used for drying shrinkage and mass-change measurements remained under these conditions, and measurements continued until 63 days. The specimens were labeled as SWx-yM, where x denotes the SW replacement level (%) and y represents the NaOH concentration.

2.4. Fresh-State Tests

The fresh-state properties of the NP-SW mixtures were examined using flow-spread and setting time tests. The flow test was used to assess how SW replacement level and NaOH concentration influenced the initial flow-spread and its retention over time. Flow was measured according to TS EN 1015-3 [26]. The truncated conical mold had an internal bottom diameter of 100 ± 0.5 mm, an internal top diameter of 70 ± 0.5 mm, and a height of

60 ± 0.5 mm, in accordance with TS EN 1015-3 [26]. The fresh mixture was placed in the conical mold and compacted. After the mold was lifted vertically, the table was dropped 15 times to allow the mixture to spread. After the mixture had spread, two perpendicular diameters were measured, and their mean was calculated as the flow diameter (D_f) using Equation (1):

$$D_f = (D_1 + D_2)/2 \quad (1)$$

Here, D_1 and D_2 are the two measured spread diameters, expressed in millimeters.

Flow was measured first at the end of mixing and then again after 15, 30, 45, and 60 min. A single fresh batch was used for each mixture. When the spread was less than 105 mm, the flow diameter could not be measured reliably; these results were therefore recorded as not measurable (NM). The 105 mm value was adopted only for this experimental program and should not be interpreted as a limit specified by a standard.

Setting times were determined using a Vicat apparatus in accordance with TS EN 196-3 [27]. The fresh mixture was placed in the Vicat mold and the top surface was leveled before testing. Setting time was measured from the point at which the precursor first came into contact with the alkaline activator. The initial setting time was defined as the time at which the distance between the needle and the base plate was 6 ± 3 mm. The final setting time was defined as the time at which the needle penetrated only about 0.5 mm into the surface. Three replicate determinations were performed for each mixture. Values are presented as means, and the error bars indicate the standard deviation (SD) of the replicate measurements (n = 3).

2.5. Physical and Mechanical Tests

The hardened NP-SW specimens were then used to determine dry bulk density, water absorption by mass, and total porosity. Prior to testing, the specimens were oven-dried at 100 °C for 24 h until constant mass was achieved, and their dry masses (m_d) were determined. Subsequently, the same specimens were immersed in water for 48 h; after the surface moisture was removed, their saturated masses (m_s) were measured. For hydrostatic weighing, the submerged masses of the specimens (m_h) were also recorded. All physical-property measurements were performed on three independent specimens for each mixture, and the results were reported as the arithmetic mean of the three specimens.

The dry bulk density (ρ, g/cm^3) of the hardened specimens was determined in accordance with TS EN 1015-10 [28] using Equation (2):

$$\rho = m_d/(m_s - m_h) \quad (2)$$

The water absorption by mass (WA, %) was determined in accordance with TS EN 13755 [29], based on the difference between the dry and saturated masses, using Equation (3):

$$WA = [(m_s - m_d)/m_d] \times 100 \quad (3)$$

The total porosity of the specimens (P, %) was calculated from the measured dry bulk density and the specific gravity of the material using Equation (4):

$$P = [1 - (\rho/\rho_s)] \times 100 \quad (4)$$

Here, ρ represents the dry bulk density of the specimen, while ρ_s represents the specific gravity. The specific gravity was determined in accordance with TS 699 [30].

Ultrasound pulse velocity measurements were performed to non-destructively assess the internal quality of the hardened specimens. The measurements were conducted using a Proceq ultrasonic testing device in accordance with TS EN 14579 [31]. The ultrasound

pulse velocity (V, km/s) was calculated as the ratio of the pulse path length to the measured transit time using Equation (5):

$$V = L/t \quad (5)$$

Here, L represents the pulse path length through the specimen, and t represents the measured transit time.

The mechanical performance of the specimens was evaluated using flexural and compressive strength tests. Three prismatic specimens from each mixture were allocated for mechanical testing. Both tests were performed in accordance with TS EN 196-1 [32] using a 2000 kN-capacity UTEST universal testing machine (UTEST Material Testing Equipment, Ankara, Türkiye). During the flexural strength test, the load was applied at a rate of 50 ± 10 N/s, whereas a loading rate of 2400 ± 200 N/s was used for the compressive strength test. Flexural strength (f_f, MPa) was determined using a three-point bending configuration and calculated from the maximum load at failure using Equation (6):

$$f_f = (1.5 \times F_f \times l)/(b \times h^2) \quad (6)$$

where F_f represents the maximum load recorded at failure (N), l represents the span between the supports (mm), b represents the specimen width (mm), and h represents the specimen height (mm).

Compressive strength (f_c, MPa) was calculated from the maximum load at failure and the loaded area using Equation (7):

$$f_c = F_c/A \quad (7)$$

where F_c is the maximum compressive load (N) and A is the loaded area (mm^2).

2.6. Drying Shrinkage and Mass Change

Drying shrinkage was monitored using the free length-change measurement approach described in TS EN 12617-4 [33], with the post-demolding conditioning regime adapted for the AAM investigated in this study. The mixtures were cast into 40 × 40 × 160 mm prismatic shrinkage molds equipped with removable metallic gauge studs. Before casting, the studs were fixed at both ends of each mold along the longitudinal axis. The mixture was then cast around them so that they remained anchored at the specimen ends after demolding. Changes in specimen length were subsequently monitored by measuring the displacement between the reference studs using an ALŞA shrinkage measurement device with a resolution of 0.001 mm. At 24 h after casting, the specimens were demolded and the initial comparator reading (L_0) was recorded; this measurement time was defined as day 0. No water-curing period was applied; the specimens were then stored at 24 ± 2 °C and 50 ± 5% relative humidity throughout the monitoring period. Three specimens were monitored for each mixture, and the reported drying-shrinkage and mass-change values represent the arithmetic mean of the three specimens. Length and mass measurements were performed at 0, 1, 3, 7, 14, 21, 28, 42, 56, and 63 days. Drying shrinkage at each measurement age was calculated using Equation (8):

$$DS_t = [(L_t - L_0)/L_g] \times 10^6 \quad (8)$$

where DS_t is the drying shrinkage at age t ($\times 10^{-6}$ mm/mm), L_0 is the initial comparator reading after demolding (mm), L_t is the comparator reading at age t (mm), and L_g is the reference gauge length between the opposing metallic gauge studs (mm). Because drying resulted in $L_t < L_0$, shrinkage values were reported as negative. At the same measurement times, the masses of the specimens were also recorded, and mass loss (ML, %) was calculated using Equation (9):

$$ML = [(m_0 - m_t)/m_0] \times 100 \quad (9)$$

where m_0 represents the specimen mass at the initial measurement, and m_t represents the specimen mass at age t.

2.7. Mineralogical Characterization, Chemical Bonding, and Pore Structure Analysis

Mineralogical phases, chemical bonds, and pore structure were characterized using XRD, FTIR, and MIP, respectively. Following the flexural strength test, each prismatic specimen was divided into two halves. One half was used for the compressive strength test. From the remaining halves, one representative fragment was selected from each of the 15 mixtures for MIP analysis. For detailed mineralogical- and chemical-bonding characterization, SW0-10M and SW30-7.5M were selected to represent the SW-free reference condition and the mixture exhibiting the most favorable overall physical and mechanical performance, respectively. XRD and FTIR analyses were conducted on the raw NP and SW materials and on fragments collected after compressive strength testing from the selected SW0-10M and SW30-7.5M specimens.

XRD analyses were performed using an XRD-6000 X-ray diffractometer (Shimadzu, Kyoto, Japan). The specimens were ground into a powder prior to analysis, and the diffraction patterns were recorded using Cu Kα radiation ($\lambda = 1.5406$ Å). The instrument was operated at 40 kV and 30 mA, and the diffraction patterns were collected over a 2θ range of 10–70°, with a scan rate of 2°/min and a step size of 0.02°.

FTIR analyses were performed at room temperature using a Bruker ALPHA II FTIR spectrometer (A250/DII, Bruker Optics GmbH, Ettlingen, Germany). The spectra were recorded over the 400–4000 cm^{-1} wavenumber range at a spectral resolution of 4 cm^{-1}, using an attenuated total reflectance (ATR) module equipped with a diamond crystal. The analyses were conducted on the raw NP and SW materials and on the selected SW0-10M and SW30-7.5M specimens to compare the silicate/aluminosilicate bonding environments before and after alkali activation.

MIP analyses were performed using an AutoPore IV 9500 mercury porosimeter (Micromeritics, Norcross, GA, USA). Prior to analysis, the specimens were dried to a constant mass, and small fragments were taken from the interior of the specimens and prepared for analysis. Measurements were conducted over a pore diameter range of 0.005–500 μm; pore diameters were calculated using the Washburn equation, assuming a mercury surface tension of 485 dyn/cm and a contact angle of 130°. From the MIP data, MIP porosity, MIP-derived average pore diameter, and the volume fractions of the different pore size ranges relative to the total intruded pore volume were determined. For detailed evaluation, the pore size distribution was classified into the ranges <0.1, 0.1–1, 1–2, 2–10, 10–100, and 100–500 μm; for the overall comparison, the main groups <0.1, 0.1–100, and 100–500 μm were used.

2.8. Environmental Assessment

A comparative material-based carbon screening was conducted to evaluate the environmental performance of the NP-SW-based AAMs. The assessment was based on the amounts of NP, solid NaOH, and waste SW used in each mixture.

For NP, an emission factor of 0.04945 kg CO_2-eq./kg was used in the baseline scenario. This value was obtained from an independently verified Type III Environmental Product Declaration (EPD) published for NP by UNACEM North America [34]. The relevant EPD uses an A1-A3 cradle-to-gate system boundary in accordance with ISO 14025 [35] and TS ISO 21930 [36] and reports a global warming potential of 49.45 kg CO_2-eq. per metric ton of NP. However, because this dataset represents a specific North American production system, it was treated in the present study as a representative factor for comparative screening rather than a site-specific emission factor for the NP used in this study.

An emission factor of 1.232 kg CO_2-eq./kg was used for NaOH, based on Yang et al. [1]. The calculation accounted for the actual amount of solid NaOH in the solution rather than the total mass of the NaOH solution. Accordingly, the 480 g portions of NaOH solution used in the 5, 7.5, and 10 M mixtures contained 81, 114, and 144 g of solid NaOH, respectively. For waste SW, a waste-allocation approach was adopted, and the production burdens associated with its previous product system were not allocated to the current assessment.

The material-based carbon indicator (C_{mat}) for each mixture was calculated as the sum of the products of the mass of each component within the assessment boundary and its corresponding emission factor, as expressed in Equation (10):

$$C_{mat} = \sum_{i=1}^{n} m_i EF_i \quad (10)$$

Here, m_i represents the mass of component i in the mixture (kg), while EF_i represents the corresponding emission factor of component i (kg CO_2-eq./kg). All C_{mat} values were calculated based on a single experimental batch containing a total of 1.2 kg of precursor.

To jointly evaluate the material-related carbon burden and mechanical performance, C_{mat} was normalized by the 28-day compressive strength to calculate the carbon intensity per unit compressive strength (CICS), as expressed in Equation (11):

$$CICS = C_{mat}/f_c \quad (11)$$

Here, f_c represents the 28-day compressive strength (MPa).

A sensitivity analysis was also performed to evaluate the effect of uncertainty in the NP emission factor on the results. In the low scenario, a value of 0.00747 kg CO_2-eq./kg was adopted from Affan et al. [37]. This value is based on an inventory that assumes, when NP-specific data are unavailable, that the impacts of NP extraction and crushing are equivalent to those of aggregate production. In the high scenario, 0.060 kg CO_2-eq./kg, corresponding to the upper limit of the 30–60 kg CO_2-eq./ton range reported in the literature for NPs, was adopted from El Inaty et al. [38]. For the baseline scenario, the value of 0.04945 kg CO_2-eq./kg obtained from the UNACEM EPD [34] was retained, and the C_{mat} and CICS values were recalculated for all 15 mixtures under the three scenarios.

A separate sensitivity analysis was conducted to examine the effect of the NaOH emission factor on the results. The C_{mat} and CICS values were recalculated for all 15 mixtures using three literature-based NaOH emission-factor scenarios: 0.633 kg CO_2-eq./kg from Thannimalay et al. [39], 1.232 kg CO_2-eq./kg from Yang et al. [1], and 1.915 kg CO_2-eq./kg from Turner and Collins [40]. The NP emission factor was held constant at 0.04945 kg CO_2-eq./kg. Because these NaOH factors originate from different geographic and inventory contexts, they are treated as alternative literature-based scenarios rather than as a statistical uncertainty interval.

For this comparative environmental assessment, the system boundary was limited to the material inputs directly used in the mixture compositions, namely NP, solid NaOH, and waste SW. The emission factors and waste-allocation approach described above were applied within this system boundary. The energy and transportation burdens associated with transporting SW from the source to the laboratory, as well as the energy used for laboratory-scale drying, grinding, and sieving, were excluded from the assessment boundary. These exclusions reflect the lack of site-specific inventory data and the study's focus on a material-input-based comparison among mixtures rather than a full life cycle assessment. Similarly, process energy associated with mixing, specimen preparation, curing, and the use of laboratory equipment was excluded from the assessment boundary. Therefore, the calculated Cmat and CICS values were interpreted not as product-level carbon footprints or full life-cycle indicators, but as material-input-based indicators for comparing all 15 mixtures under the same system boundary and allocation assumptions.

3. Results and Discussion

3.1. Fresh-State Properties

The fresh-state behavior of the mixtures was evaluated in terms of time-dependent flow-spread and initial and final setting times at varying SW replacement levels and NaOH concentrations. The flow-spread results are shown in Figure 2. In the initial measurements, mixtures without SW exhibited the highest flow-spread values within each series at all three NaOH concentrations, while the initial flow-spread gradually decreased as the SW content increased (Figure 2). This trend is clearly illustrated by the decrease in the initial spread diameter from 195 to 150 mm in the 5 M series, from 190 to 145 mm in the 7.5 M series, and from 185 to 140 mm in the 10 M series as the SW replacement increased from 0% to 40%. Because the total water content was kept constant across all mixtures, the lower flow-spread cannot be attributed to differences in total water. A plausible explanation is the finer particle-size distribution of SW compared with NP (d_{50} = 18.25 and 32.47 µm, respectively; Figure 1), which may increase the liquid demand for particle wetting and leave less free liquid available for lubrication. In addition, residual fibrous or irregular SW particles may increase interparticle friction and mechanical interlocking. Kinnunen et al. [41] discussed the fibrous nature of mineral wool as a challenge to obtaining flowable geopolymer mixtures. Accordingly, the lower flow-spread with increasing SW content may reflect both increased liquid demand and greater resistance to particle movement. Since the specific surface area and post-grinding morphology were not measured, these explanations should be regarded as plausible contributors rather than directly verified mechanisms.

The loss of flow-spread over time became more pronounced as the SW replacement level increased. For example, in the 5 M series, the spread diameter of SW0 decreased from 195 mm to 168 mm over 60 min, whereas that of SW30 decreased from 162 mm to 114 mm. Across the mixtures, most of the reduction occurred during the first 30 min, followed by a less marked decrease. After 30 min, SW40-7.5M and SW40-10M had spread diameters of 109 mm and 105 mm, respectively, and both fell below the operational measurement limit at subsequent measurement times. The NM classifications occurred for SW40-5M at 60 min, SW40-7.5M at 45 and 60 min, SW30-10M at 60 min, and SW40-10M at 45 and 60 min.

The influence of NaOH concentration was smaller than that of SW replacement. Nevertheless, at a given SW replacement level, mixtures prepared with 10 M NaOH generally had lower flow-spread values and showed a faster decrease in flow-spread over time, particularly at higher SW contents. Adewumi et al. [17] evaluated workability at different NaOH concentrations (4–14 M) in NP/limestone mortars. Because they used limestone rather than SW as the co-precursor, their findings provide only a broader context for discussing fresh-state behavior in NP-based AAMs. More directly, Yliniemi et al. [14] reported rapid reaction, high early heat release, and fast setting in NaOH-activated stone wool. These findings make reaction-related structural build-up a plausible contributor to the lower flow-spread retention observed here. However, because the cited systems differ from the present NP-SW mixtures and rheometry and calorimetry were not conducted, the mechanism underlying the observed flow loss cannot be established.

The Vicat results were consistent with the flow-spread behavior (Figure 3). In general, increasing the SW replacement level up to 30% resulted in shorter initial and final setting times at all three NaOH concentrations. For instance, in the 5 M series, initial/final setting times decreased from 168/286 min for SW0 to 124/231 min for SW30, while in the 7.5 M series, they dropped from 142/247 min to 99/192 min. A similar trend was observed in the 10 M series, where the shortest initial/final setting times, 97/181 min, were obtained for SW30-10M. However, increasing the SW replacement level to 40% led to a slight increase in setting times at all three NaOH concentrations, indicating that the relationship between SW replacement level and setting time was not monotonic. Yliniemi et al. [14] reported a

final setting time of approximately 3 h for NaOH-activated stone wool, compared with 4 h 10 min for sodium-silicate-activated stone wool and substantially longer times for sodium-aluminate- and sodium-carbonate-activated stone wool. Their results provide a relevant comparison for the present study.

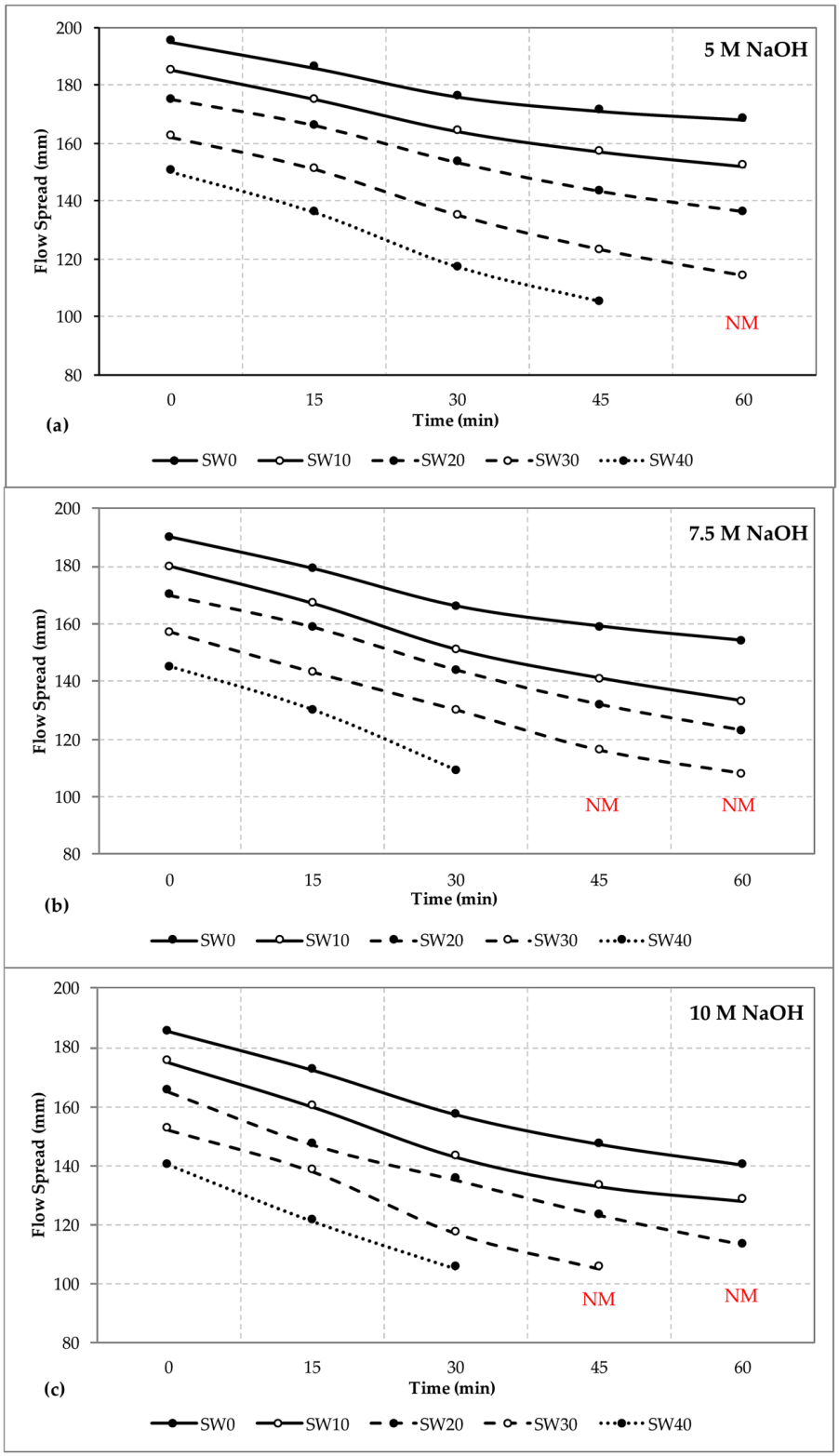


Figure 2. Time-dependent flow-spread values at varying SW replacement levels: (**a**) 5 M, (**b**) 7.5 M, and (**c**) 10 M NaOH.

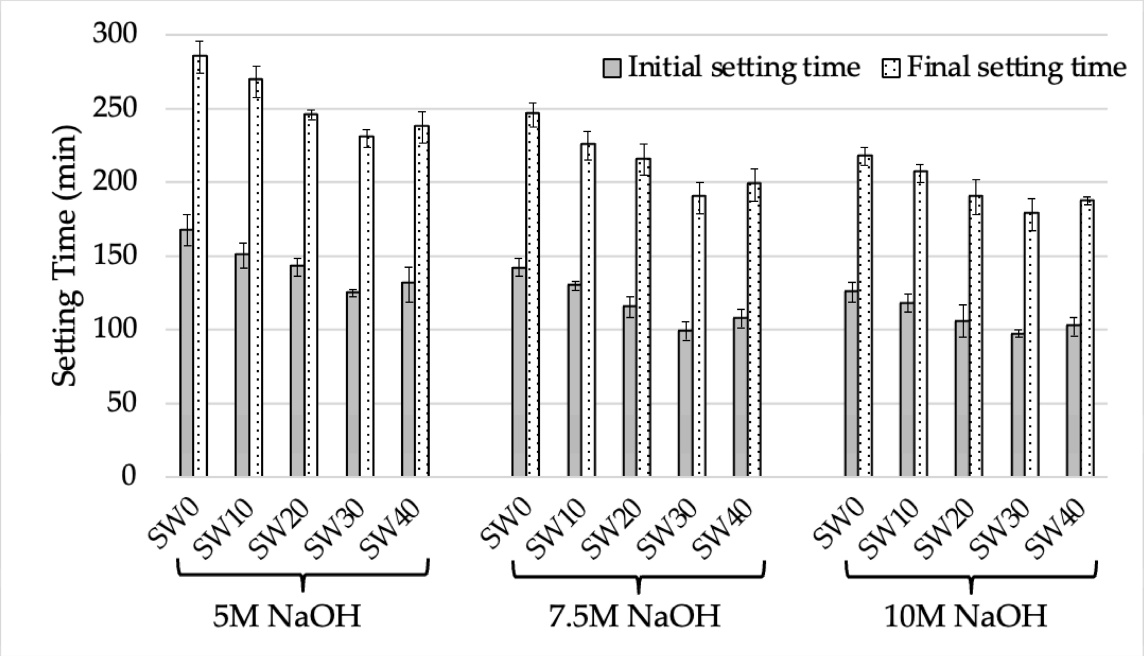


Figure 3. Effect of SW replacement level and NaOH concentration on initial and final setting times. Error bars indicate SD (n = 3).

3.2. Physical and Mechanical Properties

The effects of SW replacement level and NaOH concentration on the physical and mechanical properties of the hardened specimens are presented in Figure 4. Dry bulk density values ranged from 1.73 to 1.87 g/cm^3 (Figure 4a). In the 5 M and 7.5 M series, dry bulk density increased as the SW replacement level increased to 30%, followed by a slight decrease at 40% replacement. In contrast, in the 10 M series, the maximum value was observed at a lower SW replacement level, after which it decreased with further SW addition. These results indicate that the effect of SW content on the hardened structure depended on NaOH concentration. Porosity and water absorption by mass showed a similar trend; both decreased up to an intermediate SW replacement level and then increased at higher levels (Figure 4b,c). The lowest total porosity (15.07%) and water absorption by mass (8.32%) were recorded for the SW30-7.5M specimen. The porosity of this specimen was approximately 40% lower than that of the SW0 mixture at the same concentration, indicating that 30% SW replacement combined with 7.5 M NaOH was associated with a more densified structure. However, the increase observed at 40% SW indicates that further replacement did not result in further densification. The ultrasound pulse velocity results followed the same overall trend, with the highest value of 3.19 km/s obtained for SW30-7.5M (Figure 4d). The decrease in ultrasound pulse velocity at 40% SW was consistent with the corresponding increases in porosity and water absorption by mass. However, these physical test results alone are insufficient to attribute this behavior to a specific reaction product or pore-formation process. The relationships between these physical and mechanical properties are examined in Section 3.3, while the pore structure associated with these trends is assessed by MIP in Section 3.5.

Consistent with the trends observed in the physical properties, both flexural and compressive strengths generally increased as SW replacement rose to 30%, but decreased at the 40% replacement level for all three NaOH concentrations (Figure 4e,f). The highest flexural strength (3.41 MPa) and compressive strength (16.13 MPa) were recorded for the SW30-7.5M mixture. The compressive strength of this mixture was approximately 139% higher than that of the SW0 specimen at the same NaOH concentration. The subsequent

decline in mechanical performance at 40% SW indicates that increasing the replacement level beyond 30% did not result in further strength improvement within the investigated range. Overall, 30% SW replacement combined with 7.5 M NaOH provided the most favorable balance of physical and mechanical properties among the investigated compositions.

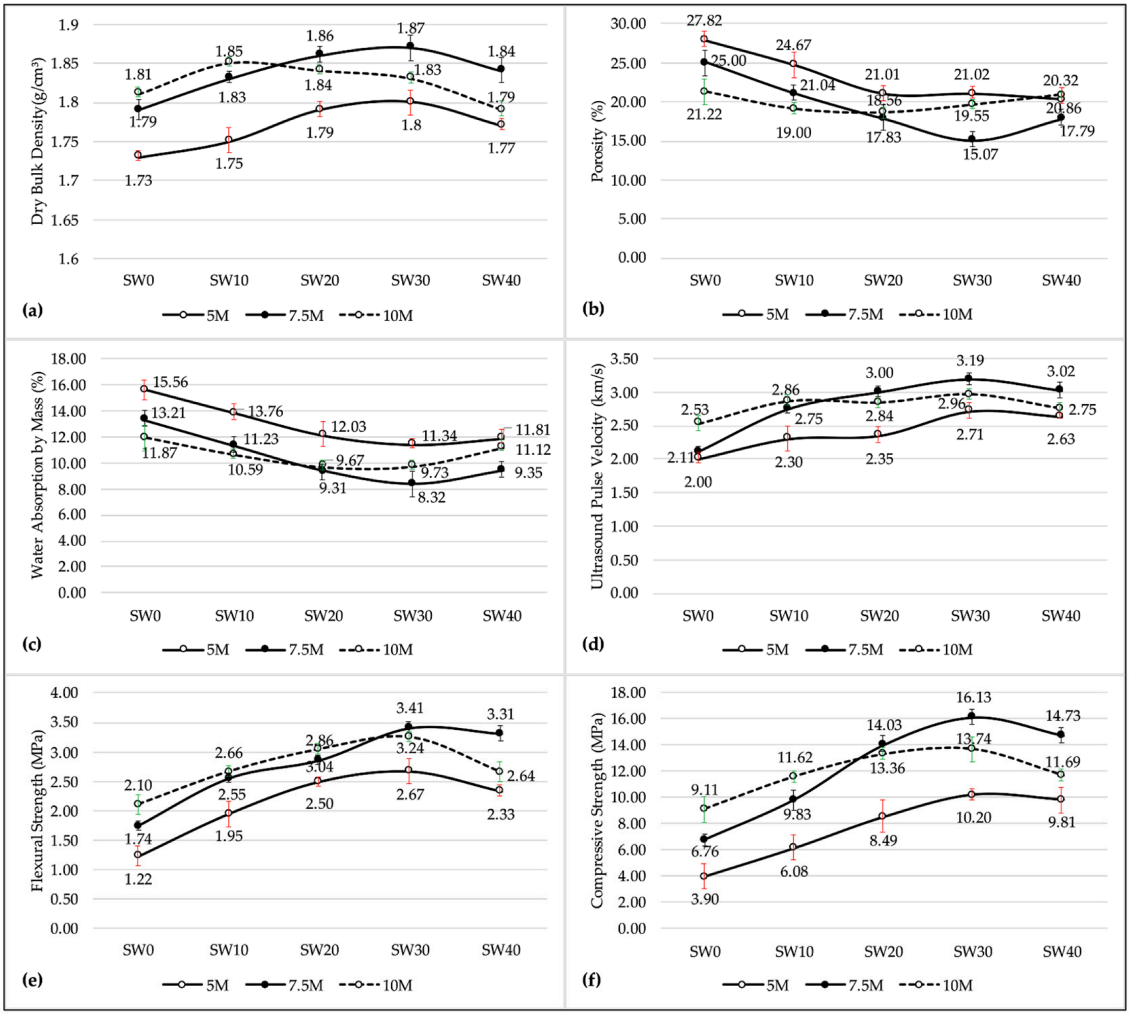


Figure 4. Effect of SW replacement level and NaOH concentration on (**a**) dry bulk density, (**b**) porosity, (**c**) water absorption by mass, (**d**) ultrasound pulse velocity, (**e**) flexural strength, and (**f**) compressive strength. Error bars indicate SD (n = 3).

The concurrent improvement in mechanical performance and physical properties at 30% SW is consistent with the formation of a denser matrix. Because SW had a finer particle-size distribution than NP (d_{50} = 18.25 and 32.47 μm, respectively), partial replacement of NP with SW may have improved particle packing at moderate replacement levels; the MIP results in Section 3.5 are consistent with this interpretation. The increase in porosity and decrease in strength at 40% SW suggest that this favorable balance was not maintained at the higher replacement level. Changes in particle packing and precursor composition may both have contributed, but their individual effects cannot be distinguished from the measurements available in this study.

The measured strengths do not establish suitability for structural applications. Based on the present results, the mixtures may be considered for future use in non-load-bearing masonry or partition products, subject to application-specific testing and verification against relevant standards.

The effect of NaOH concentration depended on the SW replacement level. In the reference mixtures without SW, increasing the NaOH concentration from 5 M to 10 M increased the compressive strength, whereas at higher SW replacement levels, the highest strengths were obtained at 7.5 M. For the SW30 mixture, compressive strengths of 10.20, 16.13, and 13.74 MPa were obtained at 5, 7.5, and 10 M, respectively. These results show that increasing the NaOH concentration did not necessarily result in higher strength and that the optimum concentration depended on the precursor composition. Similarly, Zhang et al. [25] compared 6, 8, and 10 M NaOH concentrations in volcanic ash-based AAMs. They reported the highest 28-day compressive strength, 28.3 MPa, at 8 M, followed by a decrease at 10 M. Despite differences in material composition, this trend indicates that increasing NaOH concentration beyond an optimum level does not necessarily improve mechanical performance in AAMs.

For comparison, the mechanical results were considered alongside data reported for other AAMs containing MW. Pavlin et al. [13], for example, obtained a compressive strength of about 25 MPa and a dry bulk density of 1.67 g/cm^3 for SW1. This mixture was produced entirely from waste SW activated with 5 M NaOH and cured at 40 °C for 3 days. The authors suggested that the binder formed around the remaining undissolved fibers may have contributed to the observed strength. The highest compressive strength measured in the present study was 16.13 MPa, but a direct comparison with their results would not be appropriate because the two AAMs were produced under different conditions. Pavlin et al. [13] used SW as the sole precursor, whereas SW replaced only part of the NP in the present study. The curing regimes also differed. Therefore, the difference in compressive strength cannot be attributed to NaOH concentration or SW reactivity alone. Even so, both studies indicate that SW may contribute to the mechanical performance of AAMs.

A more direct comparison can be made with the work of Luo and Yu [12], in which MWW was used to replace part of the precursor. In their fly ash-based AAMs, higher MWW replacement levels were accompanied by lower dry bulk density and higher total porosity, while the 28-day compressive strength fell below that of the reference mixture. In this study, increasing the SW replacement level to 30% led to lower porosity and higher compressive strength. This contrasting trend suggests that the effect of MWW on AAM performance depends on mixture composition and processing conditions. Its influence appears to vary with the precursor used, the amount of replacement, the activator, and the curing regime. Luo and Yu [12] also observed that higher MWW replacement levels could lower compressive strength while still improving flexural response. In this study, both compressive and flexural strengths increased as the SW replacement level rose to 30%, but declined at 40% replacement.

3.3. Relationships Between Mechanical and Physical Properties

The relationships between compressive strength and porosity, ultrasound pulse velocity, and flexural strength were examined to assess how the physical characteristics of the hardened specimens were associated with their mechanical performance (Figure 5). Compressive strength decreased as porosity increased, showing a strong linear relationship between the two parameters (R^2 = 0.9138; Figure 5a). Indeed, SW30-7.5M, which had the lowest porosity (15.07%), also showed the highest compressive strength of 16.13 MPa. Similarly, Pavlin et al. [13] reported that specimens with lower porosity generally exhibited higher mechanical strength in MW-based AAMs, although the specimens with the highest compressive and flexural strengths did not necessarily exhibit the lowest porosity. This finding supports the inverse relationship between porosity and strength observed in the present study, while also indicating that total porosity alone cannot fully explain mechanical performance.

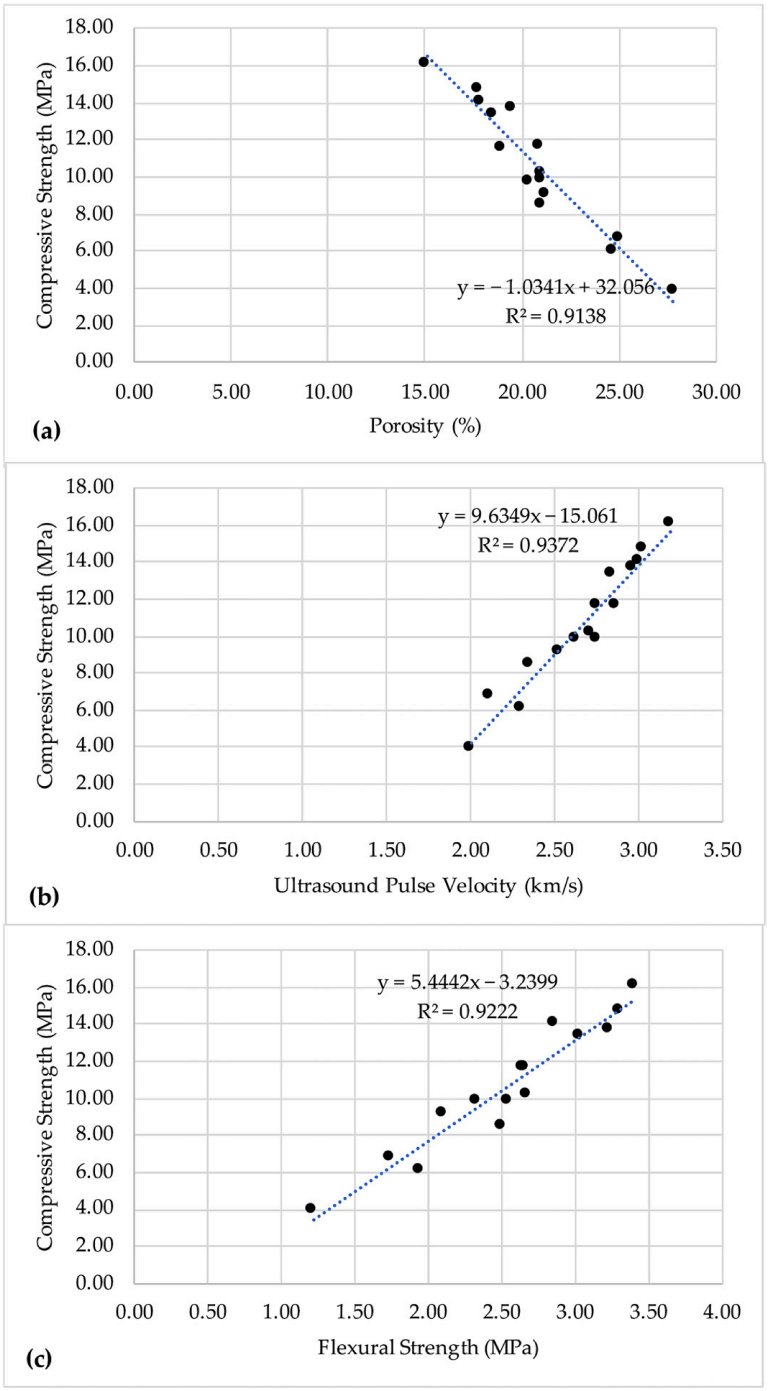


Figure 5. Relationships between compressive strength and (**a**) porosity, (**b**) ultrasound pulse velocity, and (**c**) flexural strength.

Among the three relationships examined, the strongest correlation was observed between compressive strength and ultrasound pulse velocity, with an R^2 value of 0.9372 (Figure 5b). This result indicates that specimens with higher ultrasound pulse velocity values generally exhibited higher compressive strength. This positive relationship is also consistent with the physical and mechanical trends identified in Section 3.2. Alzaza et al. [42] similarly reported that higher ultrasound pulse velocity in MW-based AAMs was associated with a denser matrix and lower air-void content. The same study also showed that increasing foam content reduced density, ultrasound pulse velocity, and both compressive and flexural strengths. Overall, the present results indicate that ultrasound pulse velocity can serve as a

useful non-destructive indicator of relative variations in mechanical performance among the investigated mixtures.

A strong positive linear relationship was also observed between compressive and flexural strengths, with an R^2 value of 0.9222 (Figure 5c). Mixtures with higher compressive strength generally exhibited higher flexural strength across the investigated SW replacement levels and NaOH concentrations. Łaźniewska-Piekarczyk and Smyczek [43] reported that the elongated MW morphology retained after grinding contributed positively to flexural strength. However, because the fiber–matrix interface and crack-bridging mechanisms were not directly investigated in the present study, the observed increases in strength cannot be attributed to a specific fiber-reinforcement mechanism. The following section examines drying shrinkage and associated mass loss, extending the evaluation of hardened-state performance to dimensional stability.

3.4. Drying Shrinkage and Associated Mass Loss

The time-dependent mass loss and drying shrinkage behavior of the mixtures are presented in Figure 6.

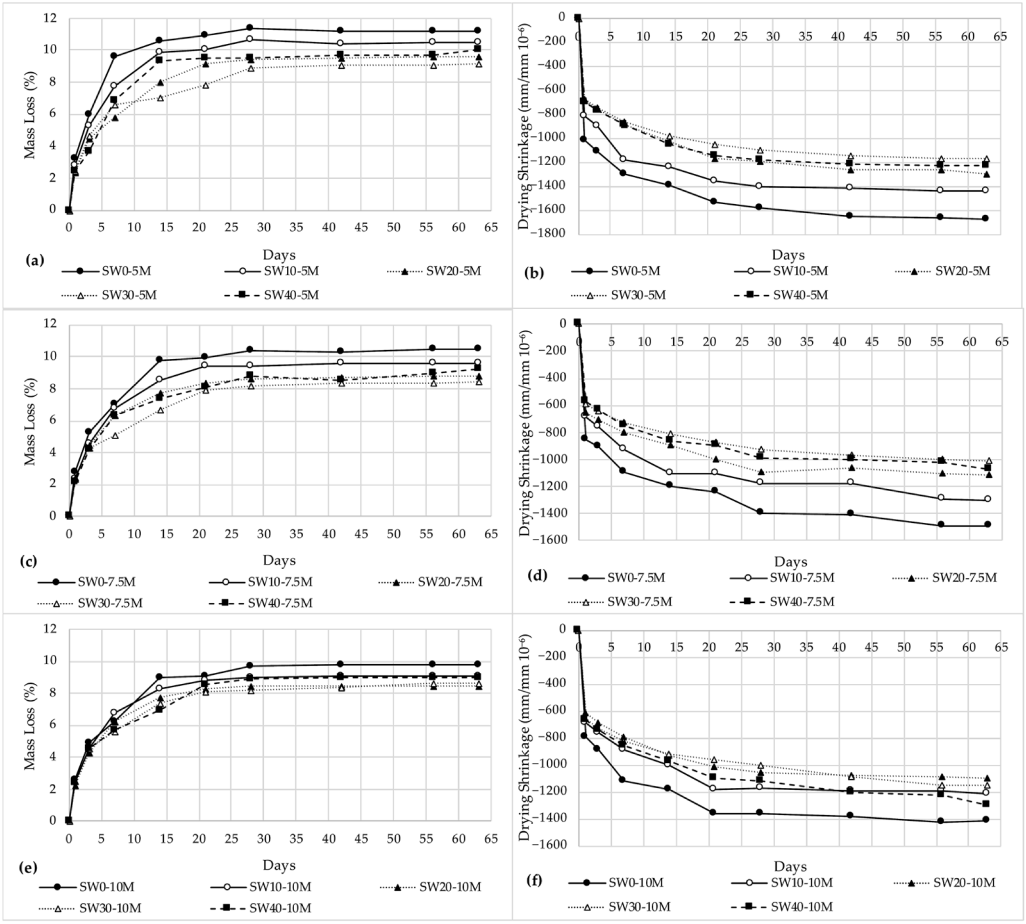


Figure 6. Time-dependent mass loss and drying shrinkage at different SW replacement levels and NaOH concentrations: (**a**,**b**) 5 M, (**c**,**d**) 7.5 M, and (**e**,**f**) 10 M NaOH.

For all mixtures, the largest changes in mass loss and drying shrinkage occurred at early ages. The rates of both processes then slowed progressively with time. Most of the mass loss took place during the first 14–28 days, after which only small additional changes were observed. Drying shrinkage showed a similar pattern, increasing rapidly during the first few weeks; however, in some mixtures, shrinkage continued to develop even after mass loss

had largely stabilized. This indicates a close relationship between shrinkage and moisture loss, while also showing that drying deformation cannot be explained by total mass loss alone. Luo and Yu [12] also reported that drying shrinkage in AAMs containing MWW followed a pattern comparable to that of drying-induced mass loss and was influenced by binder structure, reaction kinetics, and pore characteristics. Alzaza et al. [42] likewise found that most of the drying shrinkage in MW-based normal-weight AAMs developed at early ages, with approximately 90% of the maximum shrinkage reached within 14 days.

SW replacement generally reduced drying shrinkage at all three NaOH concentrations, although the effect was not linear. For instance, the shrinkage value of SW0-5M at 63 days was -1671.6×10^{-6} mm/mm, whereas smaller shrinkage magnitudes were obtained for the SW-containing mixtures. In the 7.5 M series, the lowest shrinkage magnitude was observed for SW30-7.5M, with a reported value of -1014.9×10^{-6} mm/mm. However, increasing the SW replacement level to 40% reduced this beneficial effect, particularly in the 7.5 M and 10 M series. The mass loss results generally followed the same trend, with mixtures containing moderate amounts of SW showing lower final mass losses. However, shrinkage and mass loss did not vary in parallel, suggesting that dimensional stability depends not only on the amount of water lost but also on the characteristics of the internal structure. These results are consistent with the trends reported by Luo and Yu [12], who found that the effect of MW on drying shrinkage depended on its amount and morphology. For mixtures containing longer MW fibers, shrinkage was lowest at 4% MW, but this improvement became smaller as the replacement level increased. To further examine the internal pore structure of the hardened mixtures, the MIP results are discussed in Section 3.5.

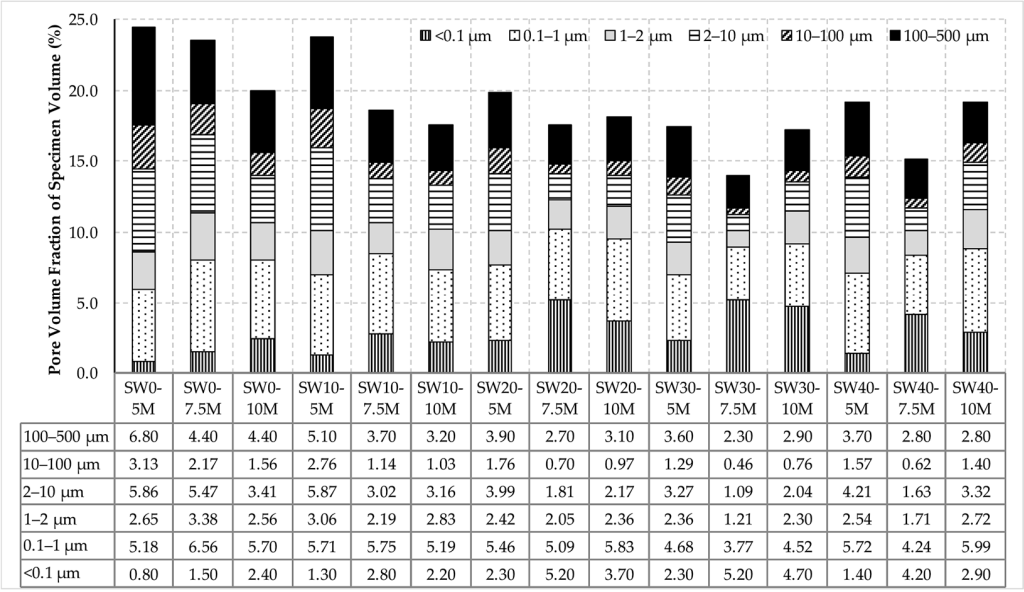
3.5. Pore Structure Characteristics

Table 3 and Figure 7 summarize the MIP results, including MIP porosity, MIP-derived average pore diameter, and the pore size distribution of each mixture. The MIP-derived porosity values should be distinguished from the total porosity values reported in Section 3.2, as the two methods are based on different measurement principles. MIP porosity ranged from 14.03% to 24.42% and generally decreased as the SW replacement level increased up to 30% at all three NaOH concentrations. The lowest MIP porosity (14.03%) was observed for SW30-7.5M, which also had an MIP-derived average pore diameter of 0.24 μm. In contrast, SW0-7.5M had an MIP porosity of 23.48% and an MIP-derived average pore diameter of 1.19 μm. The subsequent increase in MIP porosity at 40% SW indicates that the improvement in pore structure observed up to 30% replacement was not maintained at the highest replacement level. Most of the intruded pore volume in all mixtures was distributed within the 0.1–100 μm range. However, in SW30-7.5M, the proportion of pores smaller than 0.1 μm increased to 5.20%, while the proportion of pores in the 100–500 μm range remained low at 2.30%. Pavlin et al. [13] reported that lower total porosity in MW-based AAMs may occur together with a shift toward smaller pore sizes and a denser microstructure. The present results show that the physical and mechanical trends identified in Section 3.2 were also reflected in the MIP-derived pore structure. In the 7.5 M series, the increase in compressive strength from 6.76 MPa for SW0-7.5M to 16.13 MPa for SW30-7.5M coincided with lower MIP porosity and a finer pore size distribution. Luo and Yu [12] reported that MWW can modify the fine pore structure of AAMs, but that higher MWW replacement levels may also increase the proportion of larger pores.

The trends from 30% to 40% SW were consistent across all three NaOH concentrations: MIP porosity increased, while compressive strength decreased. MIP porosity increased from 17.50% to 19.14% at 5 M, from 14.03% to 15.20% at 7.5 M, and from 17.22% to 19.13% at 10 M. Over the same replacement interval, compressive strength decreased from 10.20 to 9.81 MPa, from 16.13 to 14.73 MPa, and from 13.74 to 11.69 MPa, respectively.

Table 3. MIP porosity, MIP-derived average pore diameter, and pore size distribution of mixtures with different SW replacement levels and NaOH concentrations.

Specimen	MIP Porosity (%)	MIP-Derived Average Pore Diameter (μm)	Pore Size Fraction Within Total Intruded Pore Volume (%)		
			<0.1 μm	0.1–100 μm	100–500 μm
SW0-5M	24.42	1.21	0.80	92.40	6.80
SW0-7.5M	23.48	1.19	1.50	94.10	4.40
SW0-10M	20.03	1.00	2.40	93.20	4.40
SW10-5M	23.80	1.15	1.30	93.60	5.10
SW10-7.5M	18.60	0.68	2.80	93.50	3.70
SW10-10M	17.61	0.42	2.20	94.60	3.20
SW20-5M	19.83	0.94	2.30	93.80	3.90
SW20-7.5M	17.55	0.28	5.20	92.10	2.70
SW20-10M	18.13	0.51	3.70	93.20	3.10
SW30-5M	17.50	0.83	2.30	94.10	3.60
SW30-7.5M	14.03	0.24	5.20	92.50	2.30
SW30-10M	17.22	0.27	4.70	92.40	2.90
SW40-5M	19.14	0.86	1.40	94.90	3.70
SW40-7.5M	15.20	0.25	4.20	93.00	2.80
SW40-10M	19.13	0.67	2.90	94.30	2.80



	SW0-5M	SW0-7.5M	SW0-10M	SW10-5M	SW10-7.5M	SW10-10M	SW20-5M	SW20-7.5M	SW20-10M	SW30-5M	SW30-7.5M	SW30-10M	SW40-5M	SW40-7.5M	SW40-10M
100–500 μm	6.80	4.40	4.40	5.10	3.70	3.20	3.90	2.70	3.10	3.60	2.30	2.90	3.70	2.80	2.80
10–100 μm	3.13	2.17	1.56	2.76	1.14	1.03	1.76	0.70	0.97	1.29	0.46	0.76	1.57	0.62	1.40
2–10 μm	5.86	5.47	3.41	5.87	3.02	3.16	3.99	1.81	2.17	3.27	1.09	2.04	4.21	1.63	3.32
1–2 μm	2.65	3.38	2.56	3.06	2.19	2.83	2.42	2.05	2.36	2.36	1.21	2.30	2.54	1.71	2.72
0.1–1 μm	5.18	6.56	5.70	5.71	5.75	5.19	5.46	5.09	5.83	4.68	3.77	4.52	5.72	4.24	5.99
<0.1 μm	0.80	1.50	2.40	1.30	2.80	2.20	2.30	5.20	3.70	2.30	5.20	4.70	1.40	4.20	2.90

Figure 7. MIP-derived pore size distributions of mixtures with different SW replacement levels and NaOH concentrations.

The pore size changes from 30% to 40% SW were not uniform across the NaOH concentrations. The fraction of pores smaller than 0.1 μm decreased at all three concentrations, from 2.30% to 1.40% at 5 M, from 5.20% to 4.20% at 7.5 M, and from 4.70% to 2.90% at 10 M. The MIP-derived average pore diameter changed only slightly at 5 M (0.83 to 0.86 μm) and 7.5 M (0.24 to 0.25 μm), but increased from 0.27 to 0.67 μm at 10 M. The fraction of pores in the 100–500 μm range increased slightly at 5 M and 7.5 M, but decreased slightly at 10 M. Therefore, the results indicate a reduction in the fine-pore fraction from 30% to 40% SW, but do not demonstrate a uniform increase in the largest pore fraction.

At 30% SW, MIP porosity was lowest at 7.5 M (14.03%), compared with 17.50% at 5 M and 17.22% at 10 M; this ranking was consistent with the compressive-strength results reported in Section 3.2.

The precursor characteristics provide a plausible context for interpreting these trends, although they do not establish the underlying mechanisms. SW had a finer particle-size

distribution than NP (d_{50} = 18.25 and 32.47 μm, respectively), a predominantly amorphous character, and higher CaO and MgO contents. Replacing NP with SW therefore changed both the particle-size distribution and the oxide composition of the precursor blend. The lower MIP porosity and higher fraction of pores smaller than 0.1 μm observed at 30% SW than at 40% SW are consistent with a more favorable balance of particle packing and precursor composition at this replacement level. However, the increase in MIP porosity and the decrease in strength from 30% to 40% SW indicate that this improvement was not maintained at the higher replacement level. Taken together, the measured particle-size distribution and oxide composition of SW and the MIP results suggest that the favorable performance at 30% SW reflects a balance between precursor characteristics and pore structure.

MIP alone cannot establish the chemical changes underlying these pore-structure trends; complementary XRD and FTIR results are presented in Section 3.6.

3.6. Phase and Chemical Structure Analysis

The XRD patterns of raw NP and SW, together with those of the selected AAM specimens (SW0-10M and SW30-7.5M), are presented in Figure 8. Raw SW exhibited a predominantly amorphous character, indicated by a broad diffuse-scattering region over approximately 20–35° 2θ, whereas distinct reflections assigned to quartz and anorthite were observed in raw NP. The high amorphous content of SW is consistent with previous studies; Pavlin et al. [13] reported an amorphous fraction of more than 97% in raw SW. After alkali activation, reflections assigned to quartz and anorthite remained visible in SW0-10M and SW30-7.5M, indicating that these crystalline phases were not completely consumed. Differences in the diffuse-scattering region were also observed after activation. However, because the amorphous phase content was not quantified in the present study, these patterns do not allow the degree of reaction or the amount of poorly ordered reaction products to be determined.

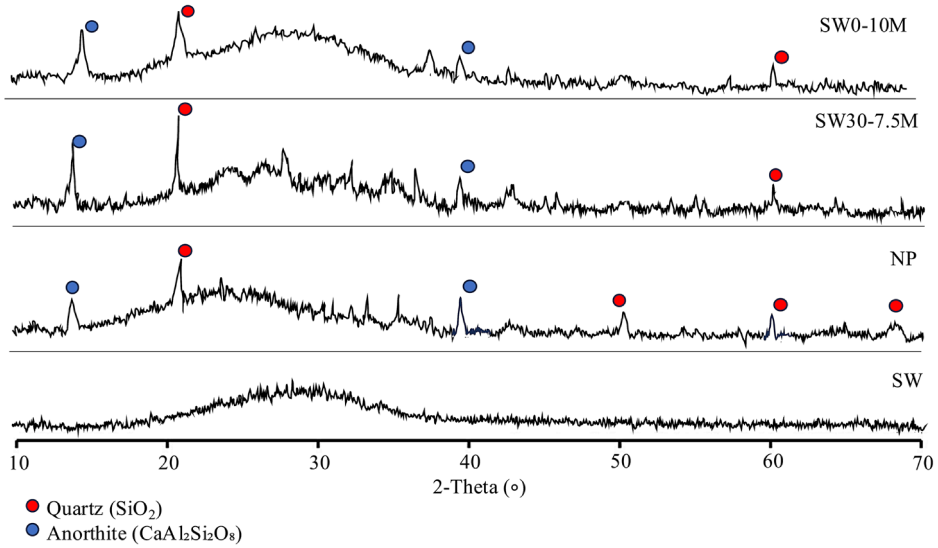


Figure 8. XRD patterns of raw NP and SW and the selected AAM specimens (SW0-10M and SW30-7.5M).

SW30-7.5M had the highest compressive strength and the most favorable MIP results among the investigated mixtures, including the lowest MIP porosity (14.03%) and MIP-derived average pore diameter (0.24 μm). However, no new dominant crystalline phase was identified in its XRD pattern. This absence is compatible with the possible presence of amorphous or poorly crystalline reaction products, but it does not demonstrate their formation or establish that they caused the improved performance. This interpretation is

consistent with reports that reaction products in SW-based AAMs may have an amorphous or nanocrystalline character [44]. Yliniemi et al. [8] investigated C-(N)-A-S-H-type binding phases in NaOH-activated SW using XRD together with scanning electron microscopy–energy-dispersive X-ray spectroscopy (SEM-EDX) and nuclear magnetic resonance (NMR) analyses. These studies provide relevant context. In addition, XRD was conducted only on SW0-10M and SW30-7.5M, which differ in both SW replacement level and NaOH concentration; the separate effects of these variables therefore cannot be isolated.

The FTIR spectra indicate changes in the silicate/aluminosilicate bonding environment after alkali activation (Figure 9). Raw SW exhibited a broad band at 905 cm^{-1} and a weaker band around 665 cm^{-1}. The 905 cm^{-1} band is consistent with the asymmetric stretching vibrations of Si–O–T (T = Si or Al) bonds reported for stone wool in previous studies [13]. The main Si–O–T band observed at 1000 cm^{-1} in raw NP shifted to approximately 980 cm^{-1} in SW0-10M and 990 cm^{-1} in SW30-7.5M after alkali activation. These shifts are consistent with changes in the original Si–O–Si and Si–O–Al bonding environments after activation. Previous studies have likewise linked shifts in the position and shape of the main T–O–T band after activation of MW-based AAMs to changes in the silicate/aluminosilicate bonding environment [13]. However, the 980 and 990 cm^{-1} positions should not be interpreted as evidence that one specimen had a higher degree of polymerization or reaction: SW0-10M and SW30-7.5M differ in both precursor composition and NaOH concentration.

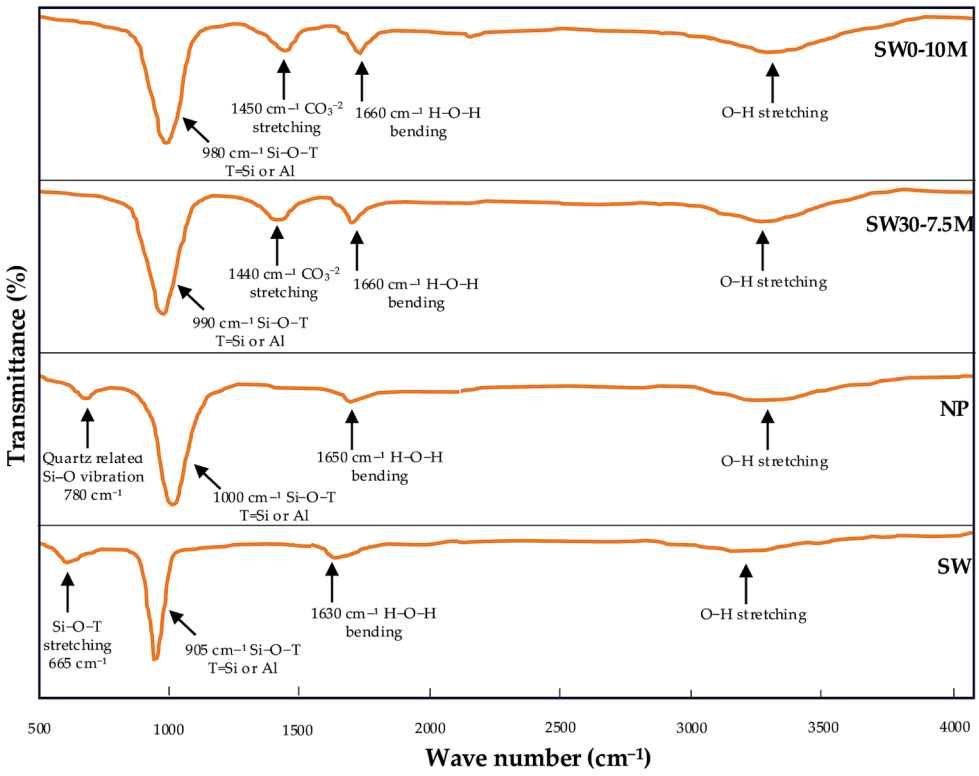


Figure 9. FTIR spectra of raw NP and SW and the selected AAM specimens (SW0-10M and SW30-7.5M).

The bands observed in the 1440–1450 cm^{-1} range in the activated specimens are attributed to the asymmetric stretching vibrations of CO_3^{2-} groups and are indicative of carbonation resulting from exposure to atmospheric CO_2. The H–O–H bending band was observed at approximately 1630 cm^{-1} in raw SW, 1650 cm^{-1} in raw NP, and 1660 cm^{-1} in the activated specimens. The broad O–H region at higher wavenumbers is associated with adsorbed water and hydroxyl-containing species [45]. Considered alongside the MIP results, the FTIR observations indicate changes in the bonding environment of the activated

specimens, while MIP and strength measurements show the favorable pore-structure and mechanical performance of SW30-7.5M. These complementary findings support a cautious association between structure and performance.

3.7. Resource Efficiency and Environmental Performance

Replacing NP with waste SW reduced NP consumption in proportion to the SW replacement level. Because the total precursor content was fixed at 1.2 kg, SW replacement levels of 10%, 20%, 30%, and 40% reduced NP use by 120, 240, 360, and 480 g, respectively. These values quantify precursor substitution and waste incorporation. They do not establish a net resource or energy benefit because the energy used for SW drying and grinding and the related transportation burdens were not quantified.

The material-input-based carbon indicators calculated within the system boundary defined in Section 2.8 are presented in Table 4. The baseline scenario results showed that, at each NaOH concentration, C_{mat} decreased as the SW replacement level increased. For instance, in the 7.5 M series, C_{mat} was 0.1998 kg CO_2-eq. for SW0, 0.1820 kg CO_2-eq. for SW30, and 0.1761 kg CO_2-eq. for SW40. Accordingly, the C_{mat} value for SW30-7.5M was approximately 8.9% lower than that of the SW0 reference at the same NaOH concentration. However, this reduction alone was not sufficient to identify the optimum mixture. Within the same series, compressive strength increased from 6.76 MPa for SW0-7.5M to 16.13 MPa for SW30-7.5M, before decreasing to 14.73 MPa for SW40-7.5M. Thus, the lowest C_{mat} value and highest compressive strength occurred at different SW replacement levels. The relationship between material-based carbon burden and compressive strength across the investigated mixtures is shown in Figure 10.

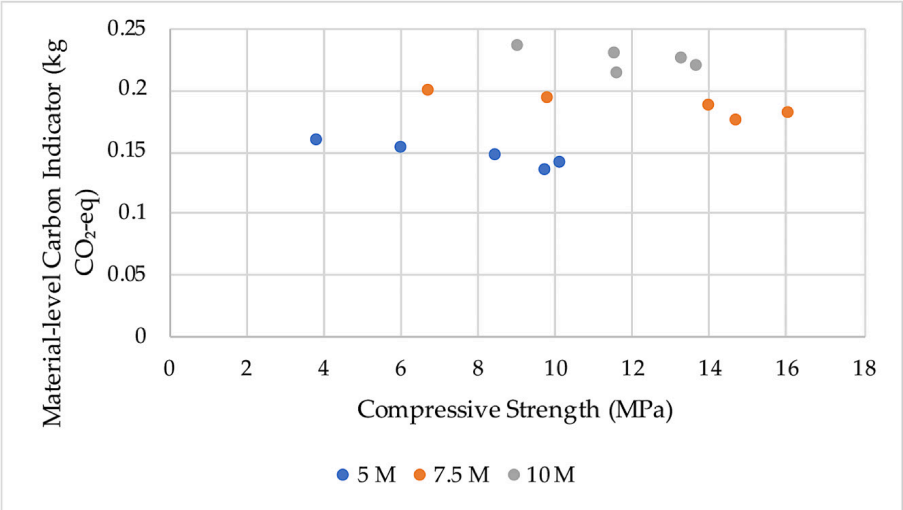


Figure 10. Relationship between the material-based carbon indicator and compressive strength for NP-SW-based AAMs at different NaOH concentrations.

The CICS values produced a different ranking from the absolute C_{mat} values. Among the 15 mixtures examined, SW30-7.5M had the lowest CICS (0.0113 kg CO_2-eq./MPa), followed by SW40-7.5M at 0.0120 kg CO_2-eq./MPa. Although SW30-7.5M did not have the lowest absolute material-based carbon indicator, it provided the most favorable balance between natural resource substitution, material-related carbon burden, and mechanical performance. In the SW30 series, increasing the NaOH concentration from 7.5 M to 10 M increased C_{mat} from 0.182 to 0.219 kg CO_2-eq., while compressive strength decreased from 16.13 to 13.74 MPa. This result shows that a higher NaOH concentration did not necessarily improve either the environmental or mechanical performance of the investigated NP-SW

mixture. Since CICS was calculated from the material-based carbon indicator of a fixed 1.2 kg precursor batch, it should be interpreted as an internal performance-normalized comparative indicator rather than a functional-unit-based life-cycle metric.

Table 4. Comparative material-based carbon and mechanical performance of NP-SW-based AAMs.

Mixture	SW Replacement (%)	NP (Kg)	SW (Kg)	Solid NaOH (Kg)	Material-Based Carbon Indicator (Kg CO_2-eq./1.2 Kg Precursor Batch)	Change Relative to SW0 at the Same NaOH Concentration (%)	Compressive Strength (Mpa)	CICS (Kg CO_2-eq./Mpa)
SW0-5M	0	1.20	0.00	0.081	0.1591	0.0	3.90	0.0408
SW10-5M	10	1.08	0.12	0.081	0.1532	−3.7	6.08	0.0252
SW20-5M	20	0.96	0.24	0.081	0.1473	−7.5	8.49	0.0173
SW30-5M	30	0.84	0.36	0.081	0.1413	−11.2	10.20	0.0139
SW40-5M	40	0.72	0.48	0.081	0.1354	−14.9	9.81	0.0138
SW0-7.5M	0	1.20	0.00	0.114	0.1998	0.0	6.76	0.0296
SW10-7.5M	10	1.08	0.12	0.114	0.1939	−3.0	9.83	0.0197
SW20-7.5M	20	0.96	0.24	0.114	0.1879	−5.9	14.03	0.0134
SW30-7.5M	30	0.84	0.36	0.114	0.1820	−8.9	16.13	0.0113
SW40-7.5M	40	0.72	0.48	0.114	0.1761	−11.9	14.73	0.0120
SW0-10M	0	1.20	0.00	0.144	0.2367	0.0	9.11	0.0260
SW10-10M	10	1.08	0.12	0.144	0.2308	−2.5	11.62	0.0199
SW20-10M	20	0.96	0.24	0.144	0.2249	−5.0	13.36	0.0168
SW30-10M	30	0.84	0.36	0.144	0.2189	−7.5	13.74	0.0159
SW40-10M	40	0.72	0.48	0.144	0.2130	−10.0	11.69	0.0182

The sensitivity analysis (Table 5) showed that changes in the NP emission factor affected the absolute environmental indicators, but SW30-7.5M remained the mixture with the lowest CICS. For SW30-7.5M, C_{mat} values were calculated as 0.1467, 0.1820, and 0.1908 kg CO_2-eq. for the low, baseline, and high scenarios, respectively, while the corresponding CICS values were 0.0091, 0.0113, and 0.0118 kg CO_2-eq./MPa. These results should be interpreted within the defined system boundary and waste-allocation approach rather than as a full life-cycle assessment. Excluding site-specific burdens associated with SW transport and preprocessing, as well as energy use during laboratory-scale processing, may affect the absolute C_{mat} and CICS values. However, the main objective of this study was to compare the 15 mixtures under the same system boundary and allocation assumptions rather than to quantify a product-level carbon footprint.

The NaOH emission-factor sensitivity analysis changed the absolute carbon indicators, while the CICS ranking remained unchanged across the 15 mixtures (Table 6). SW30-7.5M had the lowest CICS under all three scenarios, with values of 0.0070, 0.0113, and 0.0161 kg CO_2-eq./MPa for NaOH emission factors of 0.633, 1.232, and 1.915 kg CO_2-eq./kg, respectively. Its corresponding C_{mat} values were 0.1137, 0.1820, and 0.2598 kg CO_2-eq. This shows that SW30-7.5M retained the lowest CICS within the examined literature-based scenarios and the defined material-input boundary.

Table 5. Sensitivity analysis of the NP emission factor for the SW30-7.5M mixture.

NP Emission Factor Scenario	NP Emission Factor (kg CO_2-eq./kg)	SW30-7.5M Material-Based Carbon Indicator (kg CO_2-eq.)	SW30-7.5M CICS (kg CO_2-eq./MPa)
Low scenario	0.00747	0.1467	0.0091
Baseline EPD scenario	0.04945	0.1820	0.0113
High scenario	0.06000	0.1908	0.0118

Note: The low, baseline, and high NP emission factors were adopted from [34,37] and [38], respectively.

Table 6. Sensitivity of CICS to literature-based NaOH emission-factor scenarios.

Mixture	CICS at 0.633 kg CO_2-eq./kg	CICS at 1.232 kg CO_2-eq./kg	CICS at 1.915 kg CO_2-eq./kg
SW0-5M	0.0284	0.0408	0.0550
SW10-5M	0.0172	0.0252	0.0343
SW20-5M	0.0116	0.0173	0.0239
SW30-5M	0.0091	0.0139	0.0193
SW40-5M	0.0089	0.0138	0.0194
SW0-7.5M	0.0195	0.0296	0.0411
SW10-7.5M	0.0128	0.0197	0.0276
SW20-7.5M	0.0085	0.0134	0.0189
SW30-7.5M	**0.0070**	**0.0113**	**0.0161**
SW40-7.5M	0.0073	0.0120	0.0172
SW0-10M	0.0165	0.0260	0.0368
SW10-10M	0.0124	0.0199	0.0283
SW20-10M	0.0104	0.0168	0.0242
SW30-10M	0.0097	0.0159	0.0231
SW40-10M	0.0108	0.0182	0.0266

Note: CICS values are in kg CO_2-eq./MPa. The NP emission factor was held constant at 0.04945 kg CO_2-eq./kg.

4. Conclusions

The results indicate that SW replacement and NaOH concentration should be selected together. Among the mixtures examined, 30% SW combined with 7.5 M NaOH provided the most balanced performance. The decline in physical and mechanical performance at 40% SW, together with the reduction in flow-spread as SW content increased, shows that increasing the replacement level does not produce a continuous benefit. For the tested materials and mixture proportions, moderate SW replacement is therefore preferable, with flow-spread considered alongside hardened-state performance. This formulation should be regarded as the best-performing option within the investigated matrix, rather than as a universal optimum.

The measured particle-size distribution and MIP results are consistent with pore refinement contributing to the performance of the 30% SW mixture. XRD and FTIR also indicate changes in the aluminosilicate bonding environment after activation. However, these results do not establish a specific reaction mechanism: the chemical analyses covered only two mixtures that differed in both SW content and NaOH concentration, and neither a specific gel phase nor the degree of reaction was quantified.

Within the defined material-input boundary, SW replacement reduced NP consumption and the calculated C_{mat} at a given NaOH concentration. SW30-7.5M had the lowest CICS among the mixtures examined under the baseline assumptions. This ranking remained unchanged in the sensitivity analyses of the NP and NaOH emission factors. The result is limited to the material-input indicators and scenarios considered; it does not account for the energy and transportation burdens associated with SW pretreatment and delivery, and it should not be interpreted as a full life-cycle assessment.

Given the measured mechanical and dimensional-stability performance, the NP–SW AAM mixtures may warrant further evaluation for non-load-bearing masonry mortar or partition applications. Such applications were not tested in this study and would require application-specific testing, durability assessment, and verification against relevant standards. The present study was conducted at laboratory scale, involved six hours of SW grinding, and did not evaluate long-term durability. It also did not include an inferential factorial analysis to quantify the main and interaction effects of SW content and NaOH concentration. Future work should compare lower-energy SW grinding and classification methods and quantify their processing energy; evaluate each SW–NaOH combination us-

ing independently prepared replicate batches in a factorial design, supported by broader chemical and microstructural characterization, to distinguish the effects of SW dosage and NaOH concentration; and test mortar or partition elements under long-term exposure conditions and assess their compliance with relevant application standards. A process-level environmental assessment should also include site-specific pretreatment and transport data.

Funding: This work was supported by the Kocaeli University Scientific Research Projects Coordination Unit under grant number FBA-2026-5579.

Institutional Review Board Statement: Not applicable.

Informed Consent Statement: Not applicable.

Data Availability Statement: The original contributions presented in this study are included in the article. Further inquiries can be directed to the corresponding author.

Acknowledgments: The author also acknowledges the assistance provided in obtaining the volcanic tuff used in this study.

Conflicts of Interest: The author declares no conflicts of interest.

Abbreviations

The following abbreviations are used in this manuscript:

AAM	Alkali-activated material
ATR	Attenuated total reflectance
CICS	Carbon intensity per unit compressive strength
C_{mat}	Material-based carbon indicator
EPD	Environmental Product Declaration
EU	European Union
FTIR	Fourier transform infrared spectroscopy
GW	Glass wool
LOI	Loss on ignition
MIP	Mercury intrusion porosimetry
ML	Mass loss
MW	Mineral wool
MWW	Mineral wool waste
NM	Not measurable
NMR	Nuclear magnetic resonance
NP	Natural pozzolan
SD	Standard deviation
SEM-EDX	Scanning electron microscopy–energy-dispersive X-ray spectroscopy
SW	Stone wool
WA	Water absorption by mass
XRD	X-ray diffraction
XRF	X-ray fluorescence

References

1. Yang, K.H.; Song, J.K.; Song, K.I. Assessment of CO_2 reduction of alkali-activated concrete. *J. Clean. Prod.* **2013**, *39*, 265–272. [CrossRef]
2. Komkova, A.; Habert, G. Environmental impact assessment of alkali-activated materials: Examining impacts of variability in constituent production processes and transportation. *Constr. Build. Mater.* **2023**, *363*, 129032. [CrossRef]
3. Yap, Z.S.; Khalid, N.H.A.; Haron, Z.; Mohamed, A.; Tahir, M.M.; Hasyim, S.; Saggaff, A. Waste mineral wool and its opportunities—A review. *Materials* **2021**, *14*, 5777. [CrossRef] [PubMed]
4. Li, Z.; Beltran, I.A.F.; Chen, Y.; Šavija, B.; Ye, G. Early-age properties of alkali-activated slag and glass wool paste. *Constr. Build. Mater.* **2021**, *291*, 123326. [CrossRef]
5. Väntsi, O.; Kärki, T. Mineral wool waste in Europe: A review of mineral wool waste quantity, quality, and current recycling methods. *J. Mater. Cycles Waste Manag.* **2014**, *16*, 62–72. [CrossRef]

6. Karacadağ Kalkınma Ajansı. *Şanlıurfa İli Taşyünü Üretim Tesisi Ön Fizibilite Raporu*; Karacadağ Kalkınma Ajansı: Diyarbakır, Turkey, 2021. Available online: https://www.yatirimadestek.gov.tr/pdf/assets/upload/fizibiliteler/anliurfa-ili-tasyunu-uretim-tesisi-on-fizibilite-raporu—2021.pdf (accessed on 1 September 2026).
7. FAS Hansek GmbH & Co. KG. Recycling of Mineral Wool during Production Process. Available online: https://www.fas-hansek.de/technologie-2/turnkey-recycling-plants.html (accessed on 10 October 2026).
8. Yliniemi, J.; Walkley, B.; Provis, J.L.; Kinnunen, P.; Illikainen, M. Nanostructural evolution of alkali-activated mineral wools. *Cem. Concr. Compos.* **2020**, *106*, 103472. [CrossRef]
9. Adesanya, E.; Dabbebi, R.; Roößler, C.; Pavlin, M.; Li, Z.; Luukkonen, T.; Yliniemi, J.; Illikainen, M. Analysis of alkali-activated mineral wool-slag binders: Evaluating the differences between one-part and two-part variations. *J. Mater. Cycles Waste Manag.* **2024**, *26*, 1001–1011. [CrossRef]
10. Yliniemi, J.; Kinnunen, P.; Karinkanta, P.; Illikainen, M. Utilization of mineral wools as alkali-activated material precursor. *Materials* **2016**, *9*, 312. [CrossRef] [PubMed]
11. Mastali, M.; Zahra, A.; Hugo, K.; Faraz, R. Utilization of mineral wools in production of alkali activated materials. *Constr. Build. Mater.* **2021**, *283*, 122790. [CrossRef]
12. Luo, Y.; Yu, Q. Valorization of mineral wool waste in Class F fly ash geopolymer: Geopolymerization, macro properties, and high temperature behavior. *Cem. Concr. Compos.* **2024**, *145*, 105318. [CrossRef]
13. Pavlin, M.; Horvat, B.; Frankovič, A.; Ducman, V. Mechanical, microstructural and mineralogical evaluation of alkali-activated waste glass and stone wool. *Ceram. Int.* **2021**, *47*, 15102–15113. [CrossRef]
14. Yliniemi, J.; Walkley, B.; Provis, J.L.; Kinnunen, P.; Illikainen, M. Influence of activator type on reaction kinetics, setting time, and compressive strength of alkali-activated mineral wools. *J. Therm. Anal. Calorim.* **2021**, *144*, 1129–1138. [CrossRef]
15. Milat, M.; Juradin, S.; Ostojić-Škomrlj, N.; Tesovnik, A. Recycling mineral wool waste: Towards sustainable construction materials. *Recycling* **2025**, *10*, 174. [CrossRef]
16. Najimi, M.; Ghafoori, N.; Sharbaf, M. Alkali-activated natural pozzolan/slag mortars: A parametric study. *Constr. Build. Mater.* **2018**, *164*, 625–643. [CrossRef]
17. Adewumi, A.A.; Mohd Ariffin, M.A.; Yusuf, M.O.; Maslehuddin, M.; Ismail, M. Effect of sodium hydroxide concentration on strength and microstructure of alkali-activated natural pozzolan and limestone powder mortar. *Constr. Build. Mater.* **2021**, *271*, 121530. [CrossRef]
18. Robayo-Salazar, R.A.; Mejía de Gutiérrez, R. Natural volcanic pozzolans as an available raw material for alkali-activated materials in the foreseeable future: A review. *Constr. Build. Mater.* **2018**, *189*, 109–118. [CrossRef]
19. Türkmenoğlu, A.G.; Tankut, A. Use of tuffs from central Turkey as admixture in pozzolanic cements: Assessment of their petrographical properties. *Cem. Concr. Res.* **2002**, *32*, 629–637.
20. Çavdar, A.; Yetgin, Ş. Availability of tuffs from northeast of Turkey as natural pozzolan on cement, some chemical and mechanical relationships. *Constr. Build. Mater.* **2007**, *21*, 2066–2071. [CrossRef]
21. Ceylan, H. Investigation of the pozzolanic properties of Isparta Tuff. *J. Tech. Sci.* **2020**, *10*, 1–6.
22. *TS 25:2008/T1*; Natural Pozzolan (Trass) for Use in Cement and Concrete—Definitions, Requirements and Conformity Criteria. Turkish Standards Institution: Ankara, Türkiye, 2011.
23. Özata, Ş.; Akturk, B.; Yuzer, N. Utilization of waste Cappadocia earth as a natural pozzolan in alkali activation: A parametric study. *Constr. Build. Mater.* **2022**, *329*, 127192. [CrossRef]
24. Diop, M.B.; Grutzeck, M.W. Low temperature process to create brick. *Constr. Build. Mater.* **2008**, *22*, 1114–1121. [CrossRef]
25. Zhang, R.; Li, F.; Zhou, S.; Su, Y.; Liu, D.; Niu, Q. Alkali activators with different cations turning volcanic ash into eco-friendly geopolymers. *Proc. Inst. Civ. Eng. Eng. Sustain.* **2024**, *177*, 111–124. [CrossRef]
26. *TS EN 1015-3:2000/A2*; Methods of Test for Mortar for Masonry—Part 3: Determination of Consistence of Fresh Mortar (by Flow Table). Turkish Standards Institution: Ankara, Türkiye, 2007.
27. *TS EN 196-3*; Methods of Testing Cement—Part 3: Determination of Setting Times and Soundness. Turkish Standards Institution: Ankara, Türkiye, 2017.
28. *TS EN 1015-10*; Methods of Test for Mortar for Masonry—Part 10: Determination of Dry Bulk Density of Hardened Mortar. Turkish Standards Institution: Ankara, Türkiye, 2001.
29. *TS EN 13755*; Natural Stone Test Methods—Determination of Water Absorption at Atmospheric Pressure. Turkish Standards Institution: Ankara, Türkiye, 2008.
30. *TS 699*; Natural Building Stones—Methods of Inspection and Laboratory Testing. Turkish Standards Institution: Ankara, Türkiye, 2009.
31. *TS EN 14579*; Natural Stone Test Methods—Determination of Sound Speed Propagation. Turkish Standards Institution: Ankara, Türkiye, 2005.
32. *TS EN 196-1*; Methods of Testing Cement—Part 1: Determination of Strength. Turkish Standards Institution: Ankara, Türkiye, 2016.

33. *TS EN 12617-4*; Products and Systems for the Protection and Repair of Concrete Structures—Test Methods—Part 4: Determination of Shrinkage and Expansion. Turkish Standards Institution: Ankara, Türkiye, 2013.
34. UNACEM North America. *Natural Pozzolan: Manufactured at Drake Cement Plant: An Environmental Product Declaration*; UNACEM North America: Scottsdale, AZ, USA, 2025. Available online: https://www.astm.org/v3/assets/blt5eb0a2cb04534832/blt568941a3d8acc6b7/689249d343b228c5b640fe27/UNACEM_Drake_Natural_Pozzolan_EPD_2025_07_31.pdf (accessed on 11 October 2026).
35. *ISO 14025:2026*; Environmental Statements and Programmes for Products—Environmental Product Declarations (EPDs). International Organization for Standardization: Geneva, Switzerland, 2026.
36. *TS ISO 21930*; Sustainability in Buildings and Civil Engineering Works—Core Rules for Environmental Product Declarations of Construction Products and Services. Turkish Standards Institution: Ankara, Türkiye, 2021.
37. Affan, H.; Fehr, L.; Al-Massri, G.; Alassaad, F.; Yaghi, A.; Ghanem, H. Strength, transport properties, and life cycle impacts of mortar containing German Natural Pozzolan. *Infrastructures* **2026**, *11*, 67. [CrossRef]
38. El Inaty, F.; Nasreddine, H.; Djerbi, A.; Gautron, L.; Marchetti, M.; Quiertant, M.; Omikrine Metalssi, O. Mechanical and durability performance of metakaolin and fly ash-based geopolymers compared to cement systems. *Results Eng.* **2025**, *27*, 105788. [CrossRef]
39. Thannimalay, L.; Yusoff, S.; Zin Zawawi, N. Life Cycle Assessment of Sodium Hydroxide. *Aust. J. Basic Appl. Sci.* **2013**, *7*, 421–431.
40. Turner, L.K.; Collins, F.G. Carbon dioxide equivalent (CO_2-e) emissions: A comparison between geopolymer and OPC cement concrete. *Constr. Build. Mater.* **2013**, *43*, 125–130. [CrossRef]
41. Kinnunen, P.; Yliniemi, J.; Talling, B.; Illikainen, M. Rockwool waste in fly ash geopolymer composites. *J. Mater. Cycles Waste Manag.* **2017**, *19*, 1220–1227. [CrossRef]
42. Alzaza, A.; Mastali, M.; Kinnunen, P.; Korat, L.; Abdollahnejad, Z.; Ducman, V.; Illikainen, M. Production of lightweight alkali activated mortars using mineral wools. *Materials* **2019**, *12*, 1695. [CrossRef] [PubMed]
43. Łaźniewska-Piekarczyk, B.; Smyczek, D. The effect of mineral wool fiber additive on several mechanical properties and thermal conductivity in geopolymer binder. *Materials* **2024**, *17*, 483. [CrossRef] [PubMed]
44. Kurtulus, C.; Luukkonen, T. Adsorption properties of alkali-activated stone wool. *Ceram. Int.* **2025**, *51*, 1534–1545. [CrossRef]
45. Pavlin, M.; Horvat, B.; Ceˇsnovar, M.; Ducman, V. The preparation and characterization of low-temperature foams based on the alkali activation of waste stone wool. *Ceram. Int.* **2022**, *48*, 17668–17681. [CrossRef]

Disclaimer/Publisher's Note: The statements, opinions and data contained in all publications are solely those of the individual author(s) and contributor(s) and not of MDPI and/or the editor(s). MDPI and/or the editor(s) disclaim responsibility for any injury to people or property resulting from any ideas, methods, instructions or products referred to in the content.